



AIAA-94-0299

Results from the First Flight of the High Energy Imaging Device (HEIDI) Balloon Payload

C. J. Crannell, B. R. Dennis, C. C. Gaither,
F. L. Lang, L. E. Orwig, E. J. Schmahl,
R. Starr, and C. N. Hartman
NASA Goddard Space Flight Center
Greenbelt, MD

M. E. Greene and H. Tan
Auburn University
Auburn, AL

G. J. Hurford
California Institute of Technology
Pasadena, California 91125

W. N. Johnson
Naval Research Laboratory
Washington, DC

**32nd Aerospace Sciences
Meeting & Exhibit**
January 10-13, 1994 / Reno, NV

RESULTS FROM THE FIRST FLIGHT OF THE HIGH ENERGY IMAGING DEVICE (HEIDI) BALLOON PAYLOAD*

Carol Jo Crannell, Brian R. Dennis, Carl C. Gaither[†],
 Frederic L. Lang[‡], Larry E. Orwig, and Edward J. Schmahl[§]
 Solar Physics Branch, Laboratory for Astronomy and Astrophysics
 NASA Goddard Space Flight Center
 Greenbelt, Maryland 20771

Richard Starr[†]
 Astrochemistry Branch
 Laboratory for Extraterrestrial Physics
 NASA Goddard Space Flight Center
 Greenbelt, Maryland 20771

Colleen N. Hartman
 Flight Data Systems Branch
 Electrical Engineering Division
 NASA Goddard Space Flight Center
 Greenbelt, Maryland 20771

Michael E. Greene and Hong Tan
 Electrical Engineering Department
 Auburn University
 Auburn, Alabama 36849-5201

Gordon J. Hurford
 Solar Astronomy
 California Institute of Technology
 Pasadena, California 91125

W. Neil Johnson
 E. O. Hulburt Center for Space Research
 Naval Research Laboratory
 Washington, DC 20375

Abstract

Imaging solar flares in hard X rays and γ rays is the current technological and scientific frontier for solar flare physics. The objectives of the **HEIDI** (High Energy Imaging Device) Project are to develop the Fourier-transform imaging technique using rotating modulation collimators (**RMCs**) and to obtain hard X-ray and γ -ray images of solar flares and non-solar, cosmic X-ray sources such as the Crab Nebula. As currently configured, the **HEIDI** payload has two **RMCs**, one with 25-arcsecond, and the other with 11-arcsecond angular resolution; sensitivity to photon energies as high as 700 keV; and time resolution for individual photon events of 100 microseconds. It flew

for the first time on June 22, 1993, for observations of the Crab Nebula and the Sun. Engineering difficulties unfortunately prevented us from getting images of the Crab, and no solar flare above a C1.5 occurred during the six hours that the payload was at float. Analysis of the pre-flight, laser-calibration data and of the engineering data obtained during flight is now underway. The **HEIDI** effort is envisioned as part of a long-term growth plan in which **HEIDI** will serve not only as a vehicle for testing grids and associated alignment techniques being developed for the High Energy Solar Physics (**HESP**) mission, but also as a hard X-ray and γ -ray imager, ready to fly during the next solar maximum should **HESP** not come to fruition.

*Work supported in part by NASA Goddard Space Flight Center RTOP numbers 682-879-11-48 and 682-170-38-51, grant number NSG-5066 to The Catholic University of America, contract number NAS5-30792 to Caltech, contract number NAS5-30795 to Auburn University, grant number NAG5-2001 to The University of Maryland, grant number ATM-9100614 from the National Science Foundation, and grant number NL-3013U from the Arkansas Space Grant Consortium.

[†]National Research Council Postdoctoral Fellow at NASA/GSFC.

[‡]NASA Grantee through the Department of Physics, The Catholic University of America, Washington, DC 20064.

[§]NASA Grantee through the Department of Astronomy, University of Maryland, College Park, MD 20742.

I. Introduction

Development of the High Energy Imaging Device (HEIDI) balloon payload began in April 1990 as a descoped version of the Gamma-Ray Imaging Device (GRID) selected for participation in NASA's Max '91 Balloon Program. The HEIDI Project has been closely tied to our efforts in the fabrication and characterization of grids and has included the development of calibration techniques using lasers as surrogates for hard X-ray point sources. HEIDI was declared flight ready on June 17, 1993, and was flown for the first time from the National Scientific Balloon Facility (NSBF) in Palestine, Texas, on June 22. Figure 1 shows the $8.3 \times 10^6 \text{ m}^3$ (29.47 million cubic feet) balloon being filled with helium prior to launch. The telescope was pointed at the Sun for a total of more than one hour, including 25 minutes when the Sun was behind the balloon, but no hard X-ray flare occurred during the six hours at float. In the offset pointing mode, the telescope was pointed at the Crab Nebula for approximately a quarter of an hour before the balloon reached float altitude. Temperatures more than 30 degrees C colder than the design values were encountered in the electronics pressure canister during ascent, however, and subsequent problems with offset pointing prevented us from getting images of the Crab Nebula.

From an engineering standpoint, HEIDI can be viewed as a way to gain experience with the multifarious problems that must be faced and resolved before reliable and accurate images can be obtained. Questions that must be addressed include the following:

How must the grids be aligned with one another, and with the pointing and aspect systems, and with what accuracy?

How can these alignments be measured and verified during the observations?

How can the aspect of the grid system, including the azimuth or roll angle, be determined in flight for each X-ray and γ -ray photon detected?

How can all of the necessary information be obtained and recorded during the flight?

How can the data be most efficiently analyzed to produce the cleanest image without loss of information content?

All of these questions are being faced and will be answered in building, flying, refurbishing, and upgrading HEIDI. The practical experience of

struggling with the problems and finding solutions is essential for assuring the existence of a mature technology for imaging solar flares in hard X rays and γ rays for use during the next solar maximum, around the year 2000, on the High Energy Solar Physics Mission (HESP) or on balloon-borne platforms.

A description of the payload and associated technologies is presented in the following section. Results from the calibration and first flight of HEIDI are presented in Section III. Our future plans for refurbishing and reflying HEIDI are presented in Section IV.

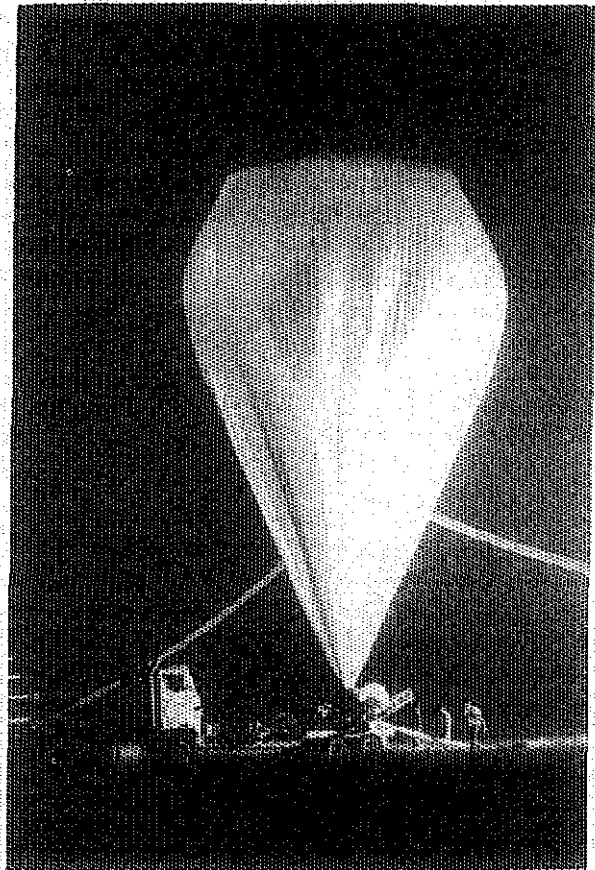


Figure 1. The balloon used to carry the HEIDI payload as it was being filled prior to flight. Photograph taken by John Herbold.

II. Payload Description

II. A. Mechanical Structures and Alignment

The primary structural components of the HEIDI payload shown in Figure 2: the gondola, canister, and metering tubes, have been described

previously (Crannell *et al.*).¹ The gondola is a welded aluminum structure 6.52 meters (21.4 ft) tall, 2.13 m (7 ft) square at its base, and 1.50 m (4.9 ft) square at the top. The canister is fabricated from titanium sheets 0.51-mm (0.02 in) thick, riveted together with 2.54-mm (0.1 in) thick reinforcing members to form an assembly 5.2 m (17 ft) long, by 0.61 m (24 in) high by 0.51 m (20 in) wide and further reinforced by four transverse aluminum bulkheads internal to the canister. The metering tubes are made of polyester fiberglass material and are nominally 5.2 m (17 ft) in length and 152 mm (6 in) in diameter with a 3.2 mm (0.125 in) thick wall. They are used as torsionally stiff metering structures that maintain parallel alignment of the grid collimators at each end with minimal twist.

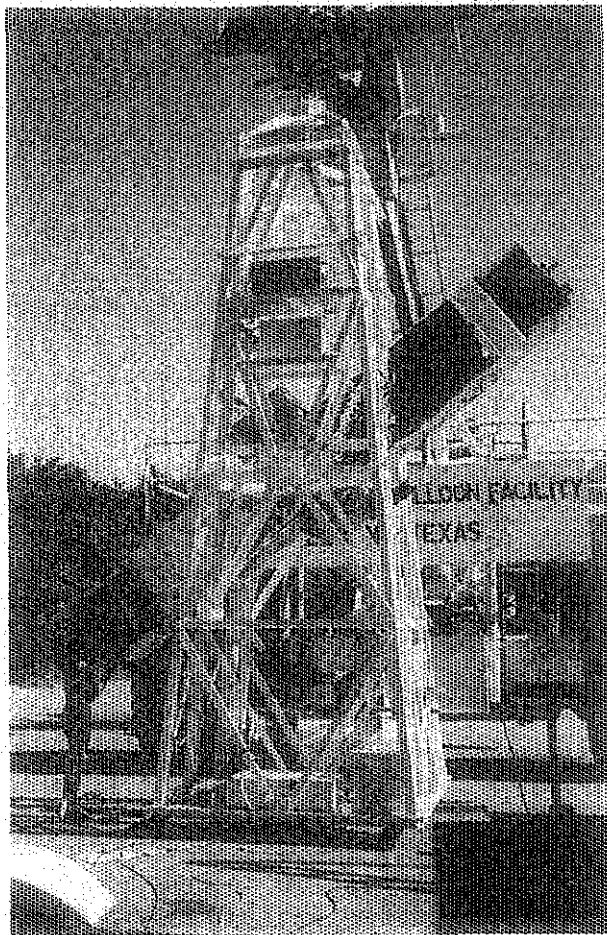


Figure 2. A photograph of the HEIDI payload during the final integration and testing phase in Palestine, Texas, prior to launch. Photograph taken by Frederic L. Lang.

The only significant change from the original design described in Crannell *et al.*¹ is the increased weight of the gondola. This resulted from the addition of several new science and engineering subsystems to the payload that necessitated reinforcements to the gondola to meet NSBF mechanical strength requirements. The actual flight weight of the gondola alone was 470 kg (1035 lb). The weight of the entire payload not including NSBF hardware was 1295 kg (2850 lb).

II. B. Imaging Optics

As described previously (Crannell *et al.*),¹ we have chosen the method of Fourier-transform imaging for the HEIDI telescope. In general, this technique is implemented with an array of one-dimensional grid collimators sensitive to different spatial frequencies in the source. The HEIDI telescope uses two rotating modulation collimators (RMCs), one with a FWHM angular resolution of 25 arcseconds, the other with 11 arcseconds. The grid pairs that form the imaging optics in each of the RMCs are spaced approximately 5.2 m apart. The four grids themselves were cut from tungsten alloy disks (92.5% W, 7.5% Ni and Fe) 130 mm in diameter and 10 mm thick using a wire electric discharge machine (WEDM). Each grid has been characterized in laboratory optical measurements, so that the positions of all the slats and slits are known relative to fiducials to an accuracy of better than 10 microns. The cumulative RMS deviation of the slats from their nominal positions has been maintained at less than 2% of the pitch, except for one fine grid, where it was 6.7%. The main physical characteristics of the four grids are summarized in Table 1.

The rotation of an RMC causes the fraction of the X-rays from a point source some distance away from the spin axis to be modulated according to a sawtooth pattern that varies in frequency depending on the orientation of the grids with respect to the direction of the source. The frequency is highest when the source appears to move perpendicular to the slits as seen from the detector and lowest, a quarter turn later, when the source appears to move parallel to the slits. An example of the expected variation in rate for one complete rotation is presented in Section III. A. At each angle of rotation of an RMC, a different point on a circle in the two-dimensional Fourier plane is sampled. Each arriving hard X-ray or γ -ray photon is time-tagged, linking its arrival to the angular position of the RMC and telescope pointing at that instant. In subsequent analysis, the

time-binned photon count rate provides the amplitude and phase of the corresponding Fourier component of the spatial distribution of the source. This modulated collimator signal, termed the "visibility" is mathematically analogous to the response of a radiowave interferometer pair in Earth-rotation synthesis.

TABLE 1.
Summary of HEIDI Grid Characteristics
(All measurements in microns)

Characteristic	Grid T	Grid R
No. of Slits	105	105
No. of Slats	104	104
Mean Pitch	1242.1	1244.8
RMS cumul. deviation	20.4	15.0
Mean Slit Width	622.7	622.8
Mean Slat Width	619.4	622.0
Mean Slit/Slat Ratio	1.005	1.001
Characteristic	Grid N	Grid P
No. of Slits	233	155
No. of Slats	232	154
Mean Pitch	559.1	565.1
RMS cumul. deviation	37.5	16.3
Mean Slit Width	330	262.0
Mean Slat Width	229	304.8
Mean Slit/Slat Ratio	1.44	0.860

Through the use of techniques well-established in radio astronomy, fairly complex distributions of sources (*e.g.*, multiple point sources, or a few extended sources) may be deconvolved from the acquired Fourier components. For single point sources, such as the Crab pulsar, a point source response function may be calculated and fit to the visibilities, thereby determining the flux and position of the source. A solar flare can produce multiple extended sources. An image can be produced from the measured visibilities using back-projection (Mertz, Nakano, and Kilner)² or the Fast Fourier Transform, followed by post-processing methods such as "CLEAN" (Högbom),³ the Richardson-Lucy algorithm (Lucy),⁴ or Maximum Entropy Deconvolution (Narayan and Nityananda).⁵

II. C. Detectors and Analog/Digital Electronics

A block diagram of the flight electronics is shown in Figure 3.

Each of the two X-ray/ γ -ray spectrometer detectors mounted on the aft end of the RMC metering tubes consists of a 90 mm diameter \times 15 mm thick NaI(Tl) scintillator and a 90 mm diameter \times 15

mm thick Schott SF1 lead glass window viewed with a 76.2 mm diameter Burle S83021EM1 photomultiplier tube (PMT) with potted bleeder string. Both assemblies include a mu-metal magnetic shield, Pb and Sn passive shielding, high-voltage power supply, and a preamplifier. The lead glass window provides an optical coupling for the NaI(Tl) scintillator light to the photomultiplier tube and also provides passive shielding in the aft direction. The energy resolution of each spectrometer is about 8% at 662 keV. The analog electronics was adjusted to provide a matched 15 to 700 keV pulse height range for each detector.

The Master Clock provides timing signals to operate all of the flight electronics systems as well as to maintain an accurate UT clock for tagging data. The heart of the system is a Conner-Winfield Model 79AX2 oven-controlled 16 MHz oscillator that was synchronized to WWVB on the launch pad and yields a clock stable to ± 3 ms per day.

The principal function of the data handling system is to accept digital data from the detector ADCs and fine aspect system, to merge these data with engineering housekeeping data, and to buffer and format these data for on-board recording on a 300 Mb Maxtor SCSI hard disk. An 80386-based on-board computer (OBC) provides the data interface to the SCSI hard disk and also serves as the parallel command interface and distribution system for the payload. A fixed sample of the total data is also formatted by a microprocessor-based telemetry formatter and an NSBF data-interface system and then telemetered to the ground in real time at a 200 kilobits/s bit rate using a bi-phase-L serial format. This capability enabled the health and safety of the payload to be monitored and provided the information for some near real-time data analysis during the mission.

The digital science-data system utilizes a photon-tagging scheme that tags each detected X-ray photon with its absolute arrival time to 0.1 ms, the energy deposited in the NaI detector with 7-bit resolution, and identification of the coarse or fine RMC detector. The channel number recorded is approximately proportional to the square root of the energy deposition. In addition, solar aspect information obtained from the fine solar aspect system is recorded with 20 ms time resolution and merged with the photon event data to produce the complete science data packet. The data handling system was designed to process up to 40,000 photon events per second per detector, which makes it well suited to handle even intense flares.

The science payload power system utilizes Eternacell lithium batteries as the primary power source. Thirteen separate stacks of various amp-hour capacities provide 17 separate unregulated voltages. Regulated subsystem voltages are generated using a combination of standard DC-DC converters and series-pass regulators. They are switched to the various subsystems using ground-commanded latching relays. The power system capacity for the first flight was sufficient for a minimum 12 hour mission. The average power required by the payload during flight is 440 Watts, and the peak power is 860 Watts. The difference is due primarily to the increase that occurs when the azimuth and elevation motors are operating at full control effort.

The science payload electronics, showing only the HEIDI flight electronics, is shown in Figure 3. Block diagram of the HEIDI flight electronics, showing only the science payload electronics systems.

The **RMC** tube drive system contains the electronics to rotate the two collimator tubes synchronously at a constant rate of 1 rev/5 s through the use of a stepper-motor-driven reduction gear and a timing-belt driver system. A system employing encoder rings and optical sensors is used to monitor the angular position and rotation speed of each of the four collimator grids. These data are collected with the on-board housekeeping data acquisition system. This dual microprocessor-controlled housekeeping system provided the monitoring of 160 analog parameters, including temperatures, battery and converter voltages, and subsystem currents. In addition, this system collects digital payload status data and merges it with the analog status to create the full set of housekeeping data.

The **OPAS** (Off-Pointing Aspect) System provides for the operation of the **OPAS** video camera and on-board **VCR** that stores the camera star field images. This system provides

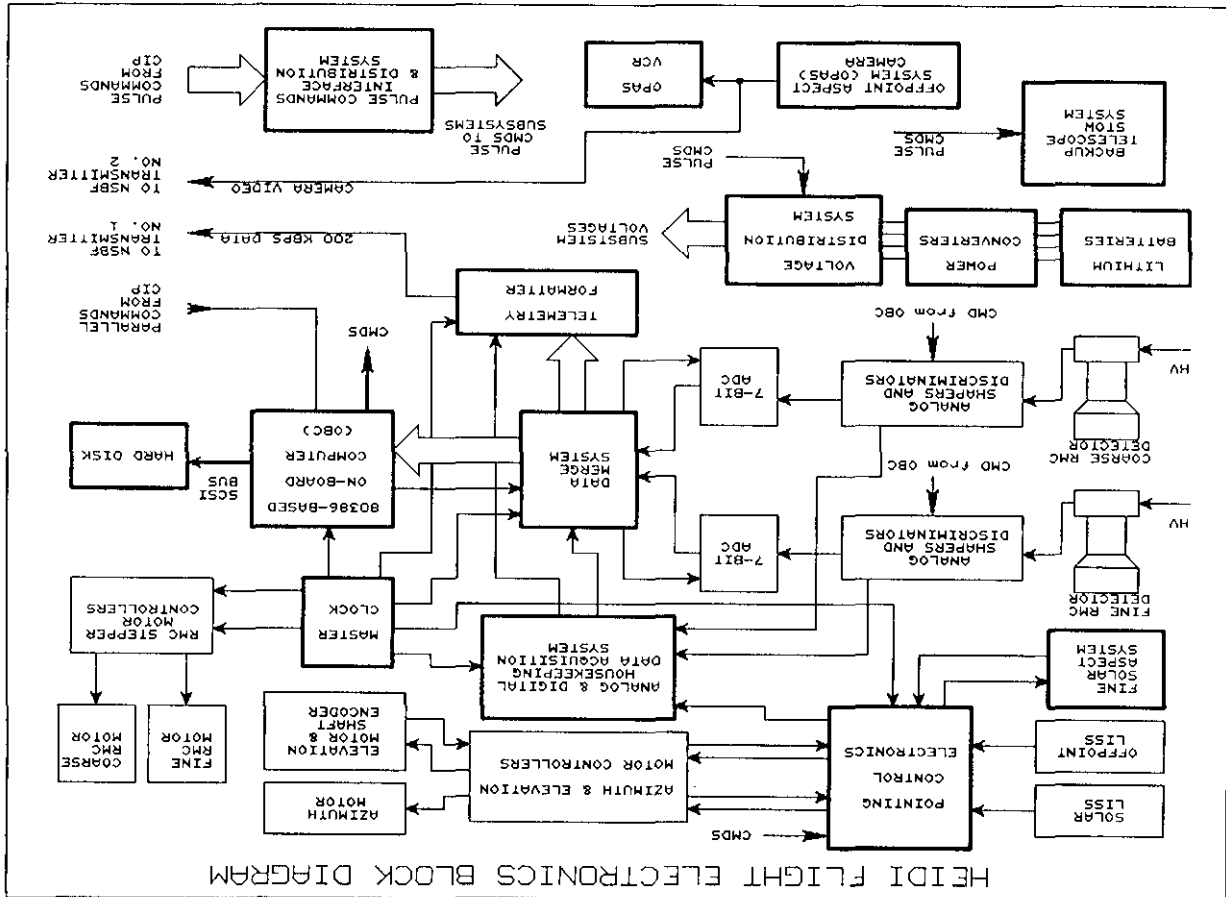


Figure 3. Block diagram of the HEIDI flight electronics, showing only the science payload electronics systems.

The final electronics subsystem is an active, closed-loop thermal control system designed to maintain the overall telescope metering structure temperature above a 0° C minimum level and also maintain the fore and aft grids to within two degrees of each other during science observations at float altitude. The system operates in a closed-loop mode using battery-powered strip heaters controlled by thermostats and a differential temperature-control circuit utilizing thermistors as the temperature sensing elements. The system could be turned on and off by ground command.

II. D. Aspect and Pointing Control

The **HEIDI** pointing control system (**PCS**) consists of a dual microprocessor-based, digital, closed-loop servo system that provides two-axis solar tracking in azimuth and elevation. It uses a directly coupled DC servo that torques against the balloon cable ladder to point in azimuth. It also uses a DC servo in elevation coupled to a 30:1 cable-driven zero-backlash gear that torques the telescope against the gondola. Both axes use Pulse Width Modulation (**PWM**) drive amplifiers operating at 2 kHz and digital controllers. Aspect input for the **PCS** is obtained with a Lockheed Intermediate Sun Sensor (**LISS**) which provides a linear error signal over a 2 degree range. Two such **LISS**es are used, one aligned with the telescope for pointing at solar sources and one deliberately offset for pointing at nonsolar sources.

Both axes also use a similar control algorithm, namely **PID** control (Proportional, Integral, Derivative). In this method, the control effort at each sample instant is summed from three terms: $K_P \times$ pointing error, $K_I \times$ integral of error, and $K_V \times$ derivative of error, where the K s are parameters of the control algorithms. The derivative term for each axis is calculated using a discrete first order current observer. The algorithms used are further subdivided into an immediate and a look-ahead calculation.

The controllers are driven by a 25 Hz hardware interrupt generated from the **LISS** signal, which supplies pointing error data. In the immediate section of the controllers, the control output is calculated for each axis. The **PWM** duty cycle is calculated and the result is loaded into the **PWM** counters. Control action is then started and the look-ahead section called.

The integral terms and velocity estimates are calculated in the look-ahead section. The output due

to these terms is then calculated for each axis and saved for the next interrupt. Between interrupts, the controller checks the mechanical limit switches and the drive current limits. It also outputs data into the **HEIDI** data collection system.

An independent fine Solar Aspect System (**SAS**), fed by two lenses (one aligned and one deliberately offset by a dual prism system), is used to provide sub-arcsecond aspect information from the solar limb for post-flight analysis of the imaging data. Both the **SAS** and **OPAS** are described in detail in Crannell *et al.*¹

II. E. Data Acquisition and Ground Support Equipment (**GSE**)

The primary function of the **GSE** MicroVAX hardware and software system is to archive data received from the payload in both ground and flight operations. The **HEIDI GSE** computer system is based on a MicroVAX 3300 minicomputer. During the pre-flight integration and test period, data from the on-board flight telemetry formatter is converted to a 16-bit parallel stream with a standard bit synchronizer and frame synchronizer and fed into the MicroVAX through a DRQ3B interface board. During flight the bi-phase bit stream from the flight telemetry formatter is transmitted to the **NSBF** receiver at the ground station at 200 kbits/s, where it is directed to the bit synchronizer as in ground operation. All data received with the MicroVAX were reformatted slightly to agree with the data format written to the on-board hard disk and were then archived to a **GSE** hard disk. Additional software was available, during both ground and flight operations, to provide page displays of engineering parameters and plots of the pointing control system performance, detector count rates, and spectral performance in near-real-time during actual operation and in playback mode from archival data files.

Pulse and 16-bit serial commands were sent to the payload by custom software running on an IBM-AT compatible computer. During ground operations of the payload, commands were sent from the command computer to the payload through a command output simulator connected directly to the on-board command interface unit via a ribbon cable. During flight operations, the commands were sent serially to the **NSBF GSE** command formatter and transmitted to the **NSBF** Consolidated Instrument Package (**CIP**) from which they were relayed to the payload command interface unit.

III. Payload Performance

III. A. Pre-launch Laser Calibration

The laser calibration of the **HEIDI RMCs** was designed to obtain data on the end-to-end throughput of the **HEIDI** hard X-ray optics. The measured point-source response function of each of the **RMCs** was obtained using a laser as a surrogate hard X-ray point source. The primary purpose of the laser calibration is to determine the effect grid imperfections, relative twist, and other instrumental characteristics have on the imaging capabilities of the instrument.

Each of the **HEIDI RMCs** was illuminated with a beam-expanded helium-neon ($\lambda = 601$ nm) laser, the light from which was then detected with a PMT substituted for the scintillation detectors. The idealized parallel wavefronts from the beam-expanded laser acted as a point source at infinity. At optical wavelengths, the **HEIDI RMCs** are diffraction limited so the telescope length was carefully chosen so that the "diffraction factor" was not near a minimum for either the coarse or the fine grids at the laser wavelength. The diffraction factor is the factor by which the modulation amplitude is multiplied to account for the effects of diffraction (Lindsey).⁶

For visible light, with a very small amount of energy per photon, the **PMTs** could not be operated in the single photon counting mode. Instead, we took advantage of the fact that, for each **RMC**, the transmitted light was modulated continuously as the **RMC** rotated. The resultant signal from the **PMT** was passed through an AC-coupled, high-pass filter that served as the input to a voltage-to-frequency converter. The output of the converter was a series of constant amplitude pulses, the frequency of which was proportional to the amplitude of the signal from the **PMT**.

These pulses from the converter were injected into the flight data system, serving as surrogate hard X-ray photon events. The top curve in Figure 4 shows a typical modulated signal obtained from the laser calibration of the coarse grids. This modulated signal is convolved with the frequency response of the high-pass filter. The middle curve in Figure 4 shows the result of removing this frequency response from the modulated signal. The bottom curve is a calculated signal determined using the instrument parameters and the known orientation of the laser beam with respect to the rotation axis of the **RMC**.

Non-uniformities in the wavefront produced by our relatively unsophisticated beam-expansion optics actually make the wavefront appear to come from a variety of different directions instead of from a point-source, as desired. Assuming that the wavefront is approximately uniform over small areas, about 20-mm diameter, we constructed masks to restrict the portion of the total beam illuminating the **RMCs**. The following data were collected for later analysis to enable the individual effects on the modulated signal due to the non-planarity of the expanded laser beam and due to the imaging quality of the instrument to be separately determined.

First, measurements were made in which only a small area of the grids was illuminated at any one time. This allows isolation of effects due to abnormalities in the grid pairs from effects due to nonuniformity of the incident wavefront. Secondly, measurements in which two small apertures at different radii were simultaneously illuminated, allowing determination of the relative twist between the grids. Additional measurements were made to determine the sensitivity and stability of the test equipment to mechanical vibrations and electronic noise.

Figure 5 shows the image of a point source created using the back-projection method (Mertz, Nakano, and Kilner)² from the modulated signal shown in Figure 4 after the effects of the high-pass filter have been removed. The large peak in the center corresponds to the position of the point source. The side lobes in this "dirty image" were removed using the CLEAN algorithm and the resulting cleaned image convolved with the point-spread function is shown in Figure 6.

Comparison of the measured modulated signals with computer-simulated modulated signals is now underway. Once the gross instrumental effects on the measured modulated signals have been determined, grid imperfections that were measured prior to flight will be incorporated in an attempt to quantitatively characterize the fine structure of the measured modulated signals. The effects grid imperfections have on the images reconstructed from these modulated signals will be investigated, also.

III. B. Grid Characterization and Alignment

A crucial ingredient for mapping with rotation collimators is the precise alignment of the fore and aft grid slats in each collimator pair. The alignment was performed several months before flight, using theodolites that enabled us to sight down the metering tubes holding the grids. The front grid was fastened

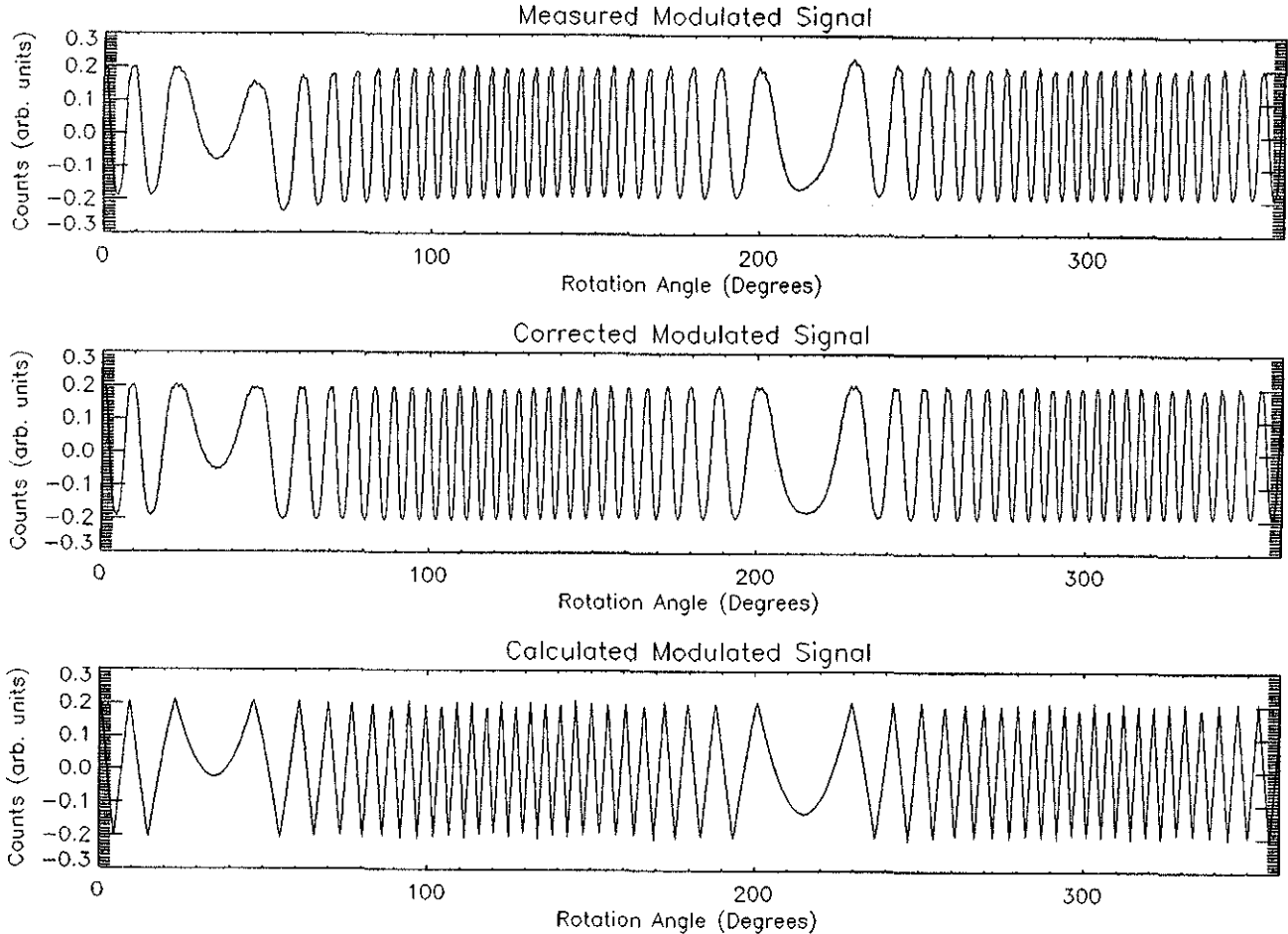


Figure 4. (Top) Measured modulated signal obtained during the laser calibration. (Middle) The same signal corrected for the frequency response of the high-pass filter. (Bottom) Calculated modulated signal incorporating telescope parameters and the known position of the laser.

to the metering tube, and the cross-hair of the theodolite was aligned with the central slit of that grid. Sighting through the forward grid, we refocused the theodolite on the aft grid, which was then rotated into alignment with the forward grid. At the pitch sizes used in these grids, there were no difficulties encountered in sighting through the grids, with the precision limited only by the resolution capability (~ 2 arcsecond) of the theodolite.

During subsequent assembly of the telescope, preparation for flight, and in flight, the relative grid twist and the rotation angles of the grids were monitored using encoder rings attached to each grid. The encoder rings each have ten non-redundantly positioned vanes with sharp edges that occult and de-occlude light emitting diodes (LEDs), the signals from which go into the data stream during rotation of the collimators. These signals have been analyzed

numerous times during construction of the telescope, in the week pre-flight, and during the flight itself. Figure 7 shows the results for short time intervals just before flight and during the flight itself. Table 2 shows the same results in numerical form.

The values of the twist measures for each collimator and diode have a different arbitrary constant (characteristic of the instrument) added in, so that only entries within a column of Table 2 may be compared, or differences of columnar variations. As shown in the Table 2's bottom line, the differences between the twist measures measured pre-flight and in-flight are less than 2.46 and 1.60 (A and B averages) for the fine and coarse collimators, respectively. The flight/pre-flight differences inferred from the A and B diodes are essentially the same, within the standard deviation (σ) of the measurement during each interval. It is worth noting that the twist variations during

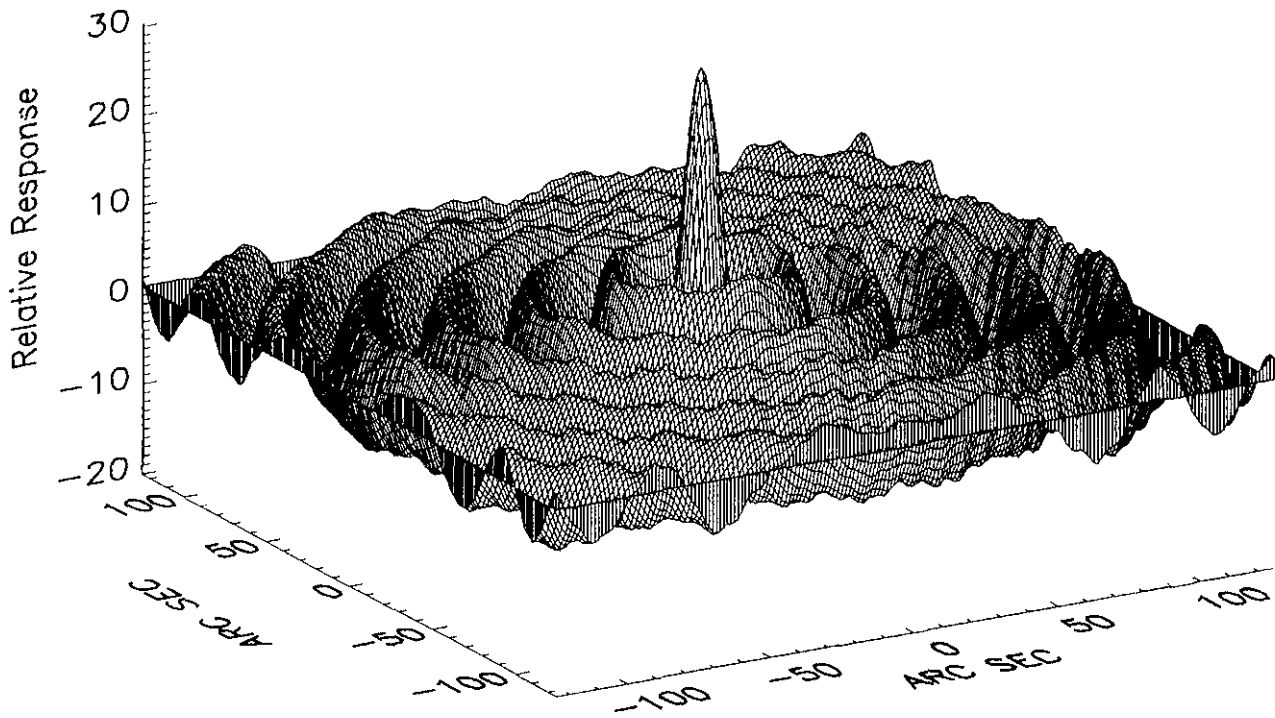


Figure 5. Surface plot of the map of the **HEIDI** image of the laser calibration source for one 360° rotation of the 25 arcsecond collimator. This image was made by backprojection (Mertz, Nakano, and Kilner)² of the recorded modulation signal multiplied by a sawtooth function of period 50 arcseconds. Note the circular “side lobes” around the central peak.

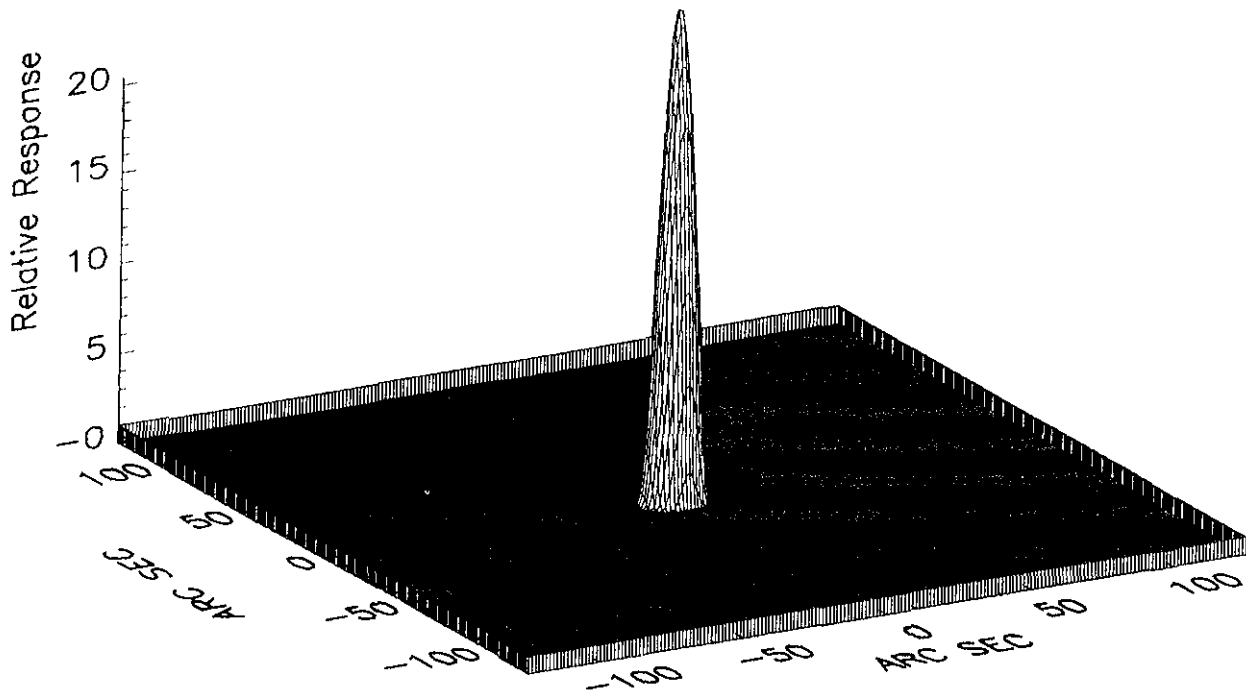


Figure 6. Surface plot of the CLEANed **HEIDI** image of the laser source, after convolution with the central lobe of the Point Spread Function. The CLEAN algorithm, a specialized version of the similar algorithm used in radio astronomy, iteratively subtracts out the side-lobes, leaving the “clean” response.

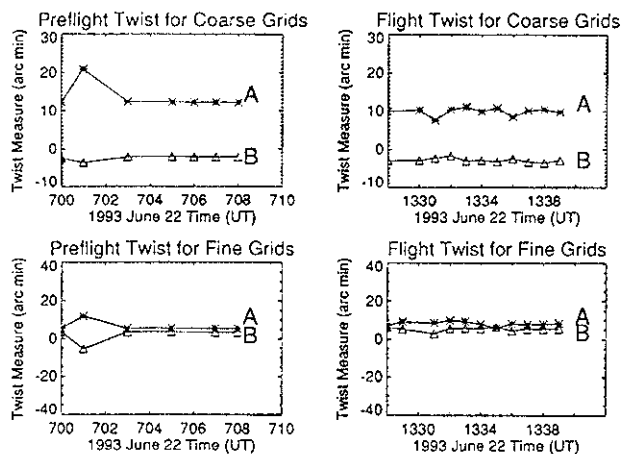


Figure 7. Plot of the collimator twist measurements derived from the preflight and flight telemetry on June 22, 1993.

TABLE 2.
Twist Measures (arcminutes)
Before and During Flight

Collimator:	11 arcseconds			
Diode Pair:	A		B	
	Mean	σ	Mean	σ
0659-0709 UT	6.33	2.37	2.22	3.40
1327-1347 UT	8.18	0.99	5.29	0.90
Difference:	1.85		3.07	
Avg. (A&B):	2.46			
Collimator:	25 arcseconds			
Diode Pair:	A		B	
	Mean	σ	Mean	σ
0659-0709 UT	13.48	3.26	-2.41	0.54
1327-1347 UT	9.80	1.01	-2.89	0.51
Difference:	-3.68		0.48	
Avg. (A&B):	1.60			

flight, as measured by σ , are smaller in each instance than during the preflight interval.

The results show that the twists of the metering tubes changed, by less than 3 arcminutes for both the fine and the coarse RMCs. For reference, a 2 arcminute relative rotation of the two grids of an RMC corresponds to a shift of 4 microns at the perimeter of a grid, or 1.4% of the slat width of the fine grids.

This gives us confidence that there was no significant relative rotation of the grids during the flight.

III. C. Detectors and Analog/Digital Electronics

During the flight of the **HEIDI** payload on June 22, 1993, the performance of the majority of the flight electronics systems was exceptionally good. The power system, RMC driver and grid position encoder system, telemetry system, payload command system, housekeeping data acquisition system, telescope thermal control system, and backup telescope stow system all operated in a nominal fashion for the entire mission. All of these systems met or exceeded their design specifications.

The detectors, high voltage power converters, and analog front-end electronics performed nominally during the flight. No gain shifts were observed in the detector spectral data, indicating that the performance of the detectors and analog electronics was stable throughout the flight. An anomaly was seen, however, in the performance of the pulse-height analysis section of the detector electronics. Figure 8 shows a typical spectrum taken with the coarse detector during flight. In addition to the expected 511-keV line, there is an unexplained spectral feature from 50 to 100 keV in both the coarse- and fine-grid detector spectra. Post-flight analysis revealed that this feature exists in pre-launch background spectra as well as in in-flight spectra of both detectors, suggesting that its origin is either in the electronics or is a real radiation effect originating in the passive Pb and Sn shield, tungsten grid, or mounting material in the proximity of the detectors. This excess of counts in the 50 to 100 keV range could adversely affect our ability to detect and image weaker sources such as our primary target for the June 1993 flight, the Crab Nebula. Prior to any future flights of the **HEIDI** payload we plan to execute a bench testing program on the detector, analog front-end, ADC, and data merge electronics to determine the origin of this unwanted spectral feature and will make efforts to eliminate the problem.

III. D. Aspect and Pointing Control Systems

The use of the Off-Pointing Aspect System (**OPAS**) and the offset pointing **LISS** for observations of the Crab Nebula required that these detectors be coaligned prior to flight. The coalignment requirements on the **LISSes** with respect to the solar aspect system were eased somewhat by the anticipated use of offset commands in the **PCS**. The most

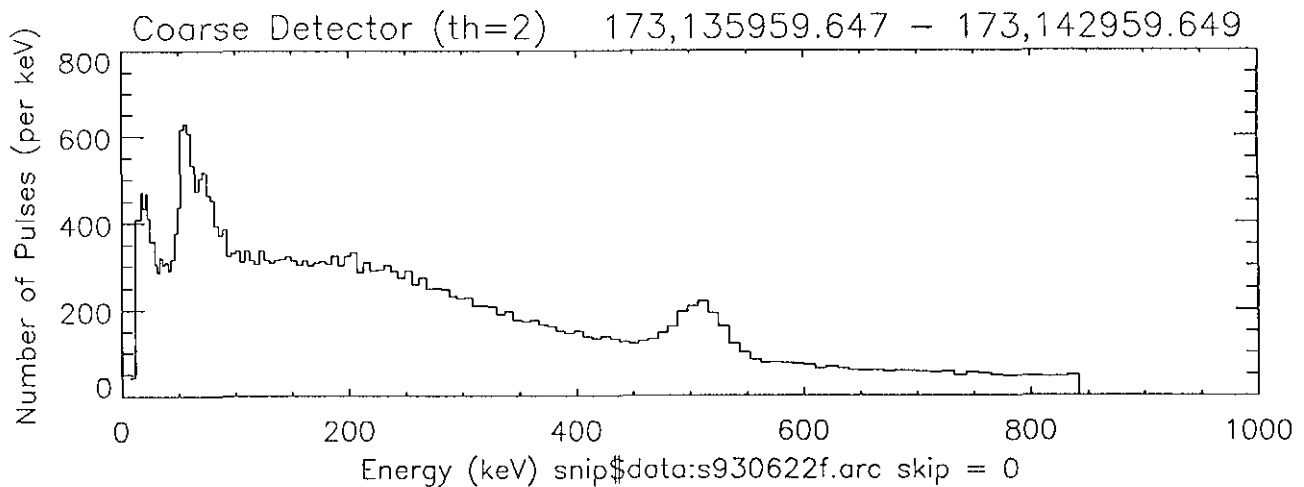


Figure 8. A 30-minute background spectrum taken with the coarse-grid detector at float altitude during the 1993 June 22 flight of **HEIDI**.

critical alignment requirement was in establishing the parameterization of the prism orientations to enable pointing to the pre-determined direction for observations of the Crab Nebula. In this case, the parameterization was established on the ground by allowing the Sun to successively drift across the fields of view of the two lenses while the canister was fixed. The known drift rate of the Sun and the precision of the aspect system was exploited to establish accurate offset parameters.

The **HEIDI** payload was launched at 1025 UT on June 22, 1993. Payload checkout was initiated during ascent, when the payload was at an altitude of approximately 30 km. The pointing control system (**PCS**) was commanded to acquire the Sun in the non-solar mode at approximately 1227 UT. Acquisition was almost immediate due to the fact that the payload was already pointing near the Sun. The video camera portion of **OPAS** showed images of the guide star Rigel, indicating that both the co-alignment of the optical systems and the pendulation of the payload were within acceptable limits.

The pointing that followed can best be characterized by three distinct phases. The first phase was one in which oscillations over the full range of the sensors in azimuth (**AZ**) predominated the pointing errors. This phase was followed by an interval in which **AZ** was quiet, but small oscillations in elevation (**EL**) occurred. The final phase was a return to phase one.

A sample of the middle period is seen in Figure 9 (**AZEL** 123900 to 124500). This interval demonstrates

several features of importance. The first is that both **AZ** and **EL** exhibit a large average control effort. In **AZ**, steady pointing required 0.42 m-kg (3 ft-lbs) or 40% of the maximum possible torque, while elevation required 1.2 m-kg (9 ft-lbs) or 30% of the maximum possible torque. These large torques were never required in testing and cannot be explained by balloon rotation or pendulation. They suggest that the bearing structures had become quite stiff.

The disturbance in the middle of the interval exhibits the characteristic of a flat spot on a bearing. The ensuing interval of oscillations in azimuth was precipitated by another such disturbance but one from which the system did not recover. Figure 10 (**AZEL** 125400 to 130000) shows the resulting pointing and control efforts. The oscillations and control efforts are consistent with a large increase in the static friction of the system. Analysis using the model developed for the system confirm these results as does Figure 11 (**AZEL** 133000-133600). The pointing data in Figure 11 were the result of our commanding an increase of a factor of two in the overall loop gain of the azimuth loop. It is interesting to note that both the amplitude and the period of the oscillations diminished. This is consistent with a stiction problem.

Approximately 20 minutes into the check-out interval, a flare alert was received in the **GOES** data provided by **NOAA**. The **PCS** was commanded into the solar pointing mode for the possible flare observations. This switch to solar mode (change of sensors) was effected successfully with no variation in

the control effort or the oscillations in azimuth and elevation.

When the flare failed to develop into a significant event, the payload was commanded back to the off-pointing mode to resume observations of the Crab Nebula. Control of the **PCS** was lost, however, probably due to low temperatures in the electronics box. A number of reacquisitions were attempted but all failed. These failures may be due in large part to the fact that acquisition was attempted in an open-loop fashion with a fixed control effort that was insufficient to rotate the payload.

A successful reacquisition is shown in Figure 12 (AZEL 174730-175400) near the end of the flight. Once again the payload was pointed almost directly at the Sun. At this time, the payload had warmed to above freezing. Note that the average AZ effort during steady pointing had fallen to about 20% of the maximum possible torque.

III. E. Thermal Control

The wide range of pressure and thermal conditions encountered during the ascent and float portions of a balloon flight present a very challenging environment for operation of the payload. This is seen clearly in Figure 13 where the external air temperature is plotted versus time for the 1993 June 22 flight of **HEIDI**. Minimum temperatures near -90° C and an average float temperatures of -40° C were encountered during the flight.

There are two major areas of the **HEIDI** payload in which thermal control of the mechanical and electronics systems is particularly crucial for optimum performance of the instrument. The first is the telescope itself, which includes the metering structure, front and rear grids, and telescope-mounted electronics systems (detectors, grid position encoder system, **RMC** motors, solar aspect system sensors, and solar and offpoint Sun sensors). The second area that requires thermal control is the interior of the aluminum pressure canister (the **PCAN**) that houses a number of key electronics subsystems: the on-board computer, hard disk, digital merge electronics, **PCS** microprocessors, and digital control electronics, half of the housekeeping data acquisition system, and the **OPAS VCR** camera. The **PCAN** is used to provide a standard-atmosphere operating environment for these systems. Thermal control of the interior of this vessel was essentially passive and was achieved by a combination of interior fans to provide a flow

of air against the walls and mounting feet of the can that radiate the heat to space. The design goal of this passive thermal control system was to maintain interior temperatures within a temperature range of 0° to $+35^{\circ}$ C during the mission.

As described in Subsection II. C., the active thermal control system developed for the telescope mechanical and electronics systems was designed to keep key structural and electronics elements above 0° C and maintain the front and rear grids within $\pm 2^{\circ}$ C of each other during the prime science observation period of the flight. This thermal control system worked very well during the flight. This is seen in Figure 13, where the flight temperature profiles of the front and rear telescope bulkhead structures are plotted. Since the front and rear bulkhead temperature monitors were mounted adjacent to the respective grids, the tungsten grid temperatures are nearly equivalent to the front and rear bulkhead temperatures. We see that the front and rear grids were maintained quite close to the $\pm 2^{\circ}$ C tolerance from 1400 UT on, covering the main science observation interval during the flight. The temperature of the front bulkhead and grid failed to meet the design goal. It fell below the 0° C minimum desired temperature from 1100 UT to 1335 UT.

Figure 13 shows the flight temperature profiles of two components of the **PCAN**. The pressure can deck is an aluminum platform on which all of the internal electronics systems are mounted. This plate is thermally well coupled to the canister exterior to help remove heat from the canister interior. The **PCS** electronics are mounted on printed circuit cards housed in a card cage that is in turn mounted to the deck. The **PCS** electronics temperature monitor is mounted in free air near one of the printed circuit cards that contains a pointing control microprocessor. As seen in Figure 13 the pressure can deck temperature dropped well below -25° C for over two hours and never got above 0° C after that. The flattening of the curve at -26° C is due to a saturation of the analog housekeeping A to D converter at the minimum of its range. The **PCS** electronics dipped to -22° C and never exceeded $+5^{\circ}$ C. Temperature monitors on other interior systems showed similar profiles. Thus, the interior systems operated in an environment significantly colder than desired. Preliminary indications are that the **PCS** electronics inside the can were adversely affected by this unexpected cold environment and that this may have been a primary contributor to the compromised performance of the **PCS** throughout the

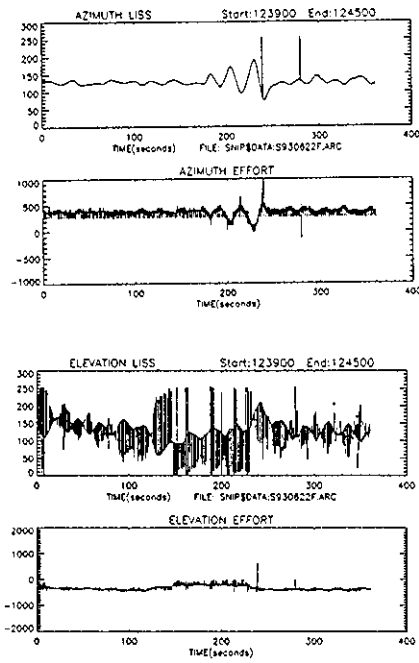


Figure 9. Quiescent pointing in the offpoint mode: (a) Azimuth LISS counts (Sun Center is at 128.); (b) Azimuth control effort (1000 units of control effort is 1.0 m-kg (7.5 ft-lbs).); (c) Elevation LISS counts (Sun Center is at 128.); (d) Elevation control effort (1000 units of control effort is 4.2 m-kg (30 ft-lbs).).

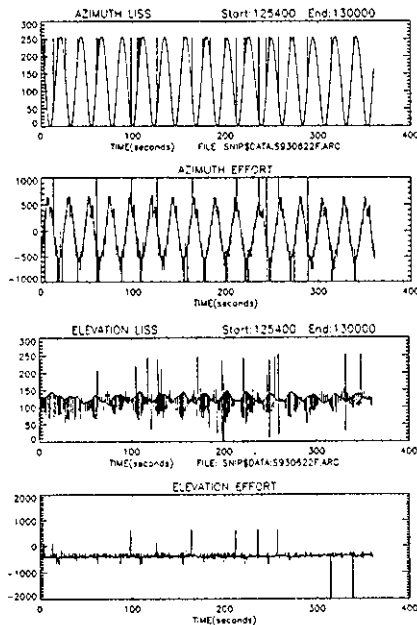


Figure 10. Pointing with oscillations in the offpoint mode: (a) Azimuth LISS counts (Sun Center is at 128.); (b) Azimuth control effort (1000 units of control effort is 1.0 m-kg (7.5 ft-lbs).); (c) Elevation LISS counts (Sun Center is at 128.); (d) Elevation control effort (1000 units of control effort is 4.2 m-kg (30 ft-lbs).).

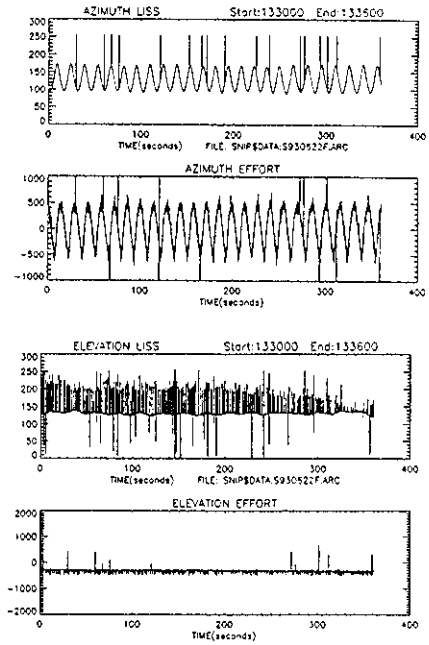


Figure 11. Pointing with increased loop gain in the offpoint mode: (a) Azimuth LISS counts (Sun Center is at 128.); (b) Azimuth control effort (1000 units of control effort is 1.0 m-kg (7.5 ft-lbs).); (c) Elevation LISS counts (Sun Center is at 128.); (d) Elevation control effort (1000 units of control effort is 4.2 m-kg (30 ft-lbs).).

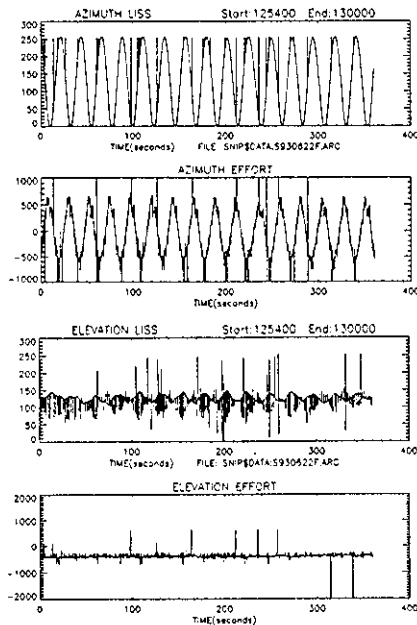


Figure 12. Successful re-acquisition in the solar pointing mode: (a) Azimuth LISS counts (Sun Center is at 128.); (b) Azimuth control effort (1000 units of control effort is 1.0 m-kg (7.5 ft-lbs).); (c) Elevation LISS counts (Sun Center is at 128.); (d) Elevation control effort (1000 units of control effort is 4.2 m-kg (30 ft-lbs).).

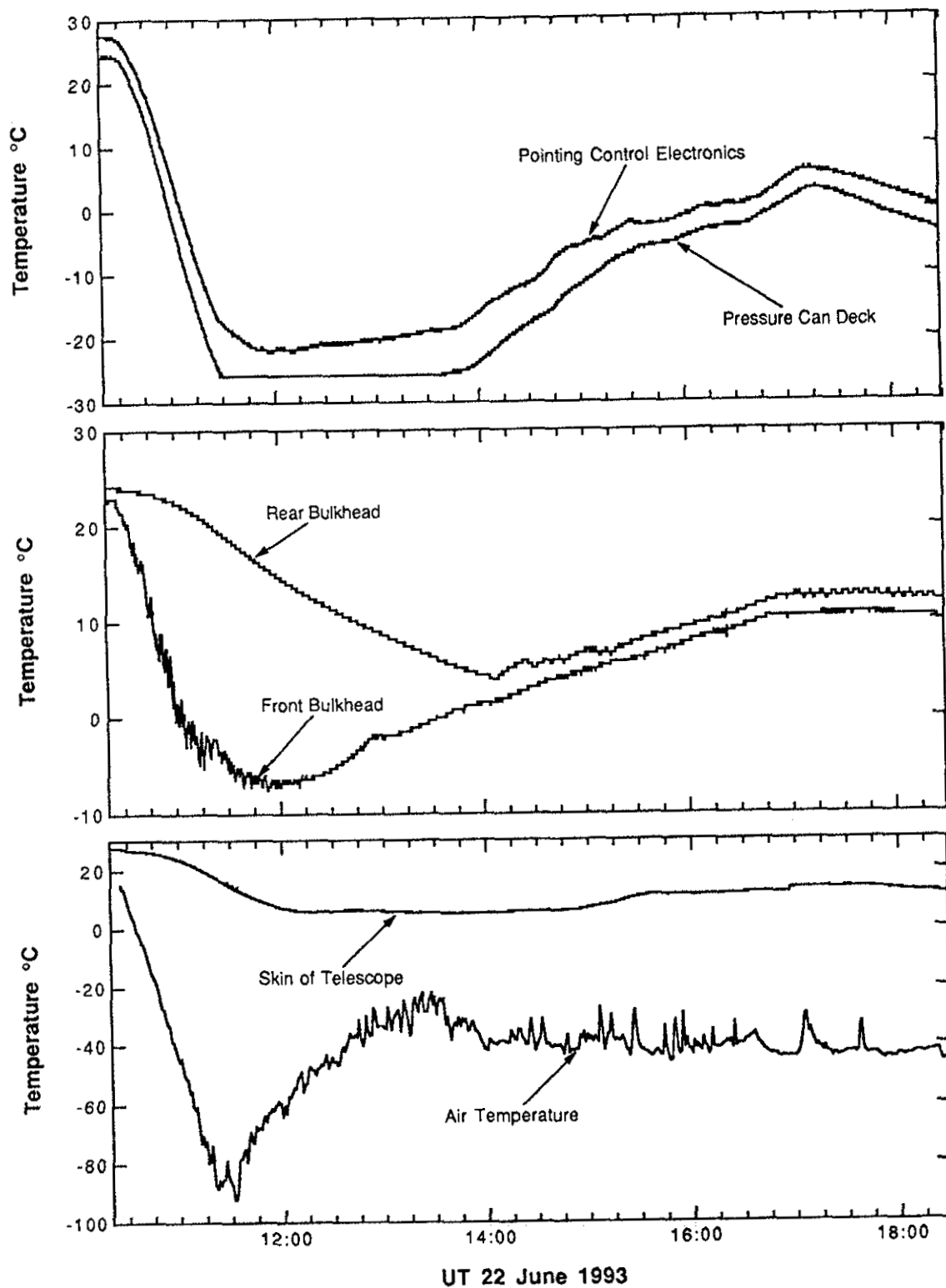


Figure 13. Profiles of the temperature *vs.* time of various **HEIDI** payload systems measured during the 1993 June 22 flight: A - pointing control electronics card cage and aluminum mounting deck inside the electronics pressure canister; B - front and rear telescope bulkheads (or front and rear tungsten grids) of the telescope; C - temperature of the telescope's titanium skin and the free air temperature (as measured by an **NSBF**-provided monitor mounted beneath the payload).

flight. The remaining electronics systems inside the **PCAN** appeared to have operated nominally at these unexpectedly low temperatures.

This thermal problem will be corrected using the following approach. We will repeat the thermal modelling of the electronics pressure can to better understand of the cause of the discrepancy between the anticipated thermal profile and the profile actually observed during flight. In these new calculations, we will use the flight temperature and power dissipation data as inputs to the model. In order to achieve more control of the thermal environment, we will install a system of battery-powered strip heaters inside the pressure can which can be either thermostatically controlled on board or controlled from the ground by command. Such a system will provide a simple solution to the cold temperature problem inside the electronics pressure can.

III. F. Data Acquisition and GSE

The primary function of the **HEIDI GSE**, both during ground operations and during flight, was to archive the data as they were received. This system performed flawlessly, except during brief intervals of telemetry dropout. Timely display of engineering parameters during both ground and flight operation of the **HEIDI** payload was deemed extremely desirable in order to monitor the health of the payload, the performance of the **PCS**, and the scientific potential and content of the observations. The current **GSE** computer system proved somewhat inadequate to satisfactorily meet these latter goals. The page display software lagged only a few seconds behind real time, and was generally adequate to monitor gross properties of the operation of the instrument. The plotting software, on the other hand, was capable of processing only about one minute of data for every two minutes of elapsed time, too great a delay to meet our goals of near-real-time visual inspection of the pointing-control system performance and detector count rates and spectral performance.

The command computer system also worked flawlessly in flight with over 450 commands being sent without a single error.

IV. Summary and Future Plans

The continued effort for **HEIDI** is envisioned as part of a long-term growth plan in which **HEIDI** will serve not only as a vehicle for testing grids and associated alignment techniques being developed for the High Energy Solar Physics (**HESP**) mission, but

also as a hard X-ray and γ -ray imager ready to fly during the next solar maximum should **HESP** not come to fruition. Over the next three years, this will involve image-reconstruction simulations and software development, analysis of both calibration and flight data, hardware refurbishment and development, and two reflights of the **HEIDI** payload.

Reflight in FY '95 is being approached conservatively with the principal goal being to refurbish the payload and reduce the risk of failures in flight. New 8.3-arcsecond grids, now being developed in collaboration with **JPL**, will replace the present 11-arcsecond grids; and 130-mm diameter detectors will replace the original 90-mm diameter ones.

The **HEIDI** payload has been built to support as many as four **RMCs** extending to angular resolutions as fine as 2 arcseconds. For the reflight in FY '96, a third **RMC** will be added to the telescope using two independently rotating grids with optical encoders, similar to those now employed for diagnostic purposes only, and a servo system to keep them aligned. This will enable us to test even finer grids, selected from those now being developed as part of the **HESP** study, and provide experience implementing **RMCs** with optical encoders as elements in an active servo system.

VI. Bibliographical References

- ¹C. J. Crannell, B. R. Dennis, L. E. Orwig, E. J. Schmahl, F. L. Lang, R. Starr, J. P. Norris, M. E. Greene, G. J. Hurford, W. N. Johnson, and K. S. Wood, "A Balloon-Borne Payload for Imaging Hard X Rays and Gamma Rays from Solar Flares", Proceedings of the "AIAA International Balloon Technology Conference," held in Albuquerque, New Mexico, 1991 October 8-10, AIAA-91-3653 (1991) 1-11.
- ²L. N. Mertz, G. H. Nakano, and J. R. Kilner, "Rotational Aperture Synthesis for X Rays", *J. Opt. Soc. Am.* **3** (1986) 2167.
- ³J. A. Högbom, *Astron. Astrophys. Suppl.* **15** (1974) 417.
- ⁴L. B. Lucy, *Astron. J.* **79** (1974) 745.
- ⁵R. Narayan and R. Nityananda, *Ann. Rev. Astrophys.* **24** (1986) 127.
- ⁶C. A. Lindsey, "Effects of Diffraction in Multiple-Grid Telescopes for X-Ray Astronomy", *J. Opt. Soc. Am.* **68** (1978) 1708.